RESEARCH

Heterogeneous angularly colliding (Al–Cu) laser-produced plasmas and film deposition

S. Shilpa[1] · Pramod Gopinath[1,2]

Abstract
The dynamics of heterogeneous angularly colliding (Al–Cu) laser-produced plasmas with varying input laser pulse energies on each target are studied using fast imaging and optical emission spectroscopic techniques. The stagnation layer formed at the collision front consists of both Al and Cu species, and its intensity varied with the variation in laser pulse energy. Multispecies stagnation region formation and the variation of spectral line intensity with laser pulse energy are studied using the optical emission spectroscopic technique. The depositions of interaction regions are analyzed using the XRD, EDAX, FESEM, and AFM techniques. The intermetallic compound formation is possible using this technique, and the composition can be varied by varying the input laser pulse energies. The major benefits are the flexibility of controlling parameters and the simplicity of experimental setup for the formation of intermetallic compounds. Thus, angular target geometry for colliding laser-produced plasma is proposed to efficiently mix different metals with control over the composition of deposited films.

1 Introduction

Laser-produced plasmas have attracted the curiosity of researchers for several decades due to its broad range of applications, including laser-induced breakdown spectroscopy (LIBS) [1], pulsed laser deposition (PLD) [2] for thin film growth [3], inertial confinement of fusion [4], and microelectronics fabrication [5]. Most of the applications of laser-produced plasmas can be improved using colliding plasmas. The presence of another plasma plume at the collision front can significantly influence the nature and effect of a single plasma plume. There exist two extreme possibilities of plasma interaction at the collision front. High-density plasmas with low relative velocity can stagnate at the collision front, forming a dense layer called the stagnation region. In contrast, low-density plasmas with high relative velocity possess a greater tendency for interpenetration. Another exciting factor is the possibility of several controlling parameters on the collision dynamics that make the colliding plasma more special. The parameters which can alter the collision characteristics include target geometry, inter-plume separation, seed plasma parameters, and ambient gas [6–9]. Studies on the colliding laser-produced plasmas (CLPP) provide an experimental basis for many astrophysical phenomena [10] and serve to increase our knowledge about the collision processes in indirectly driven inertial confinement fusion reactors [11]. Using CLPP, we can improve the signal-to-background ratio of LIBS studies [12]. Another important application is in PLD, where dual pulse PLD or cross-beam PLD can significantly improve the quality of film deposition [13].

Several researchers have investigated the parametric influence on the collision dynamics of plasmas, whereas very few focus on the collision dynamics of plasmas from two different target materials [14]. The effect of the target angle on the stagnation layer formed by the collision of aluminum and silicon was studied by Al-Juboori et al., and reported that the length of the stagnation layer increases with the decrease of wedge angle [15]. Pandey et al. studied the lateral collision dynamics of copper and titanium at different oxygen ambient pressures [16]. These studies were extended to deposition of nanocomposites at different pressures [17].

Most of the studies focus on the influence of ambient gas pressure on the properties of films. The engineering properties of the stagnation layer can also be effectively utilized in deposition techniques. Tuning of incident laser

✉ Pramod Gopinath
   pramod@cusat.ac.in

1   International School of Photonics, Cochin University of Science and Technology, Kochi 682022, India

2   Inter University Centre for Nanomaterials and Devices, Cochin University of Science and Technology, Kochi 682022, India

pulse energy can alter the composition and properties of the deposited film, which is an advantage of using a heterogeneous colliding system. The two simultaneously ablated metals have a possibility of getting mixed up in the colliding region [18]. Metal alloys that are very useful but difficult to manufacture can be effectively prepared using this technique. Al–Cu is one of the most significant alloys of Al used in different fields such as aircraft construction, space technology and in automobiles, due to its excellent mechanical properties and high strength-to-weight ratio. Al–Cu alloys are difficult to manufacture due to the difference in physical and chemical properties of the base metals [19, 20]. The interaction region formed at the collision front of heterogeneous colliding plasmas of Al and Cu can be effectively used for the preparation of a combination of both metals. By varying the input laser pulse energy on the individual metal targets, we can control the stoichiometry of the mixture.

Studies focused on the collision dynamics of heterogeneous colliding plasmas and its utility are very limited. It is essential to explore the complex collision dynamics of two different targets with great differences in all its properties. In the case of angular target geometry, it is expected to have a better collision of individual seed plasmas resulting in excellent mixing of metals. In the present work, we report the dynamics of angularly colliding aluminum and copper plasmas by varying the input laser pulse energy on each target and the study of film deposition and its variation.
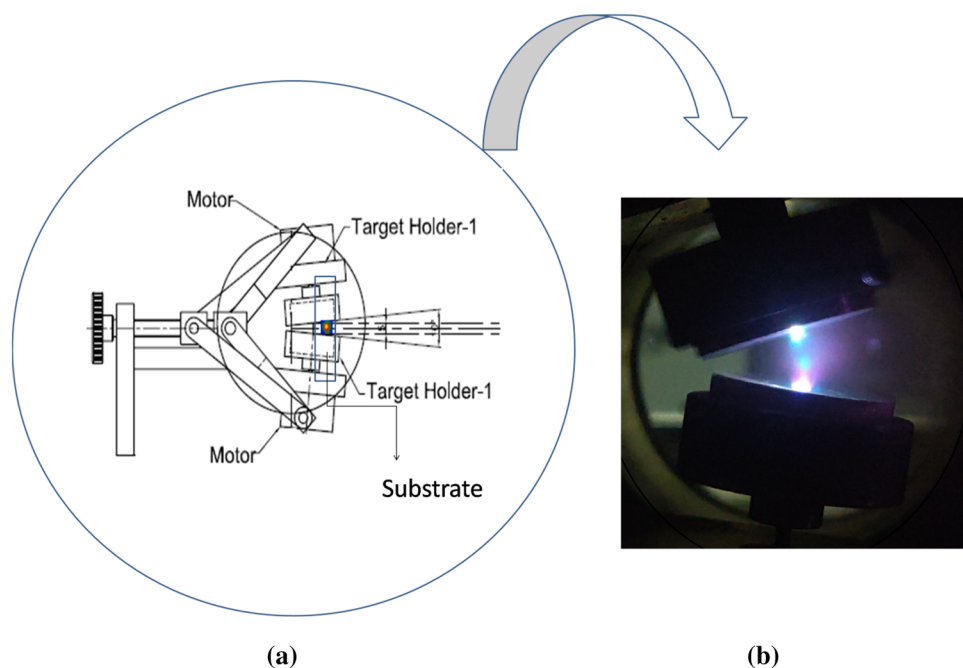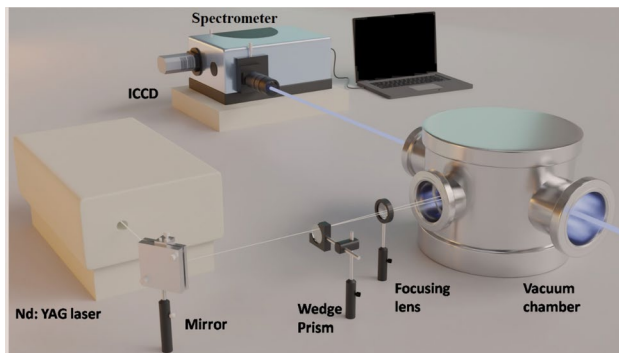
2 Experimental setup

The heterogeneous colliding plasma is produced using a Q-switched Nd:YAG laser of pulse width 10 ns and a repetition rate of 10 Hz operating at its fundamental wavelength of 1064 nm and an energy of 130 mJ, split into two using a wedge prism of 2° 5′ 56″ wedge angle. The two laser pulses are allowed to focus on two different targets using a focusing lens with a focal length of 60 cm. The two targets consist of Aluminum and Copper kept at an angle of 40^0, and the two seed plasmas are at a separation of 9 mm. The two targets are rotated using two separate motors to avoid surface etching. The schematic diagram of the target holder and the direct photograph of collision is shown in Fig. 1 and the details of the experimental setup are given in our previous work [8, 9]. The glass substrate is kept 3 cm away from the interaction region in an off-axis position. Undesirable contamination of the film can be avoided by keeping the substrate in off-axis position. All these set up is kept in a vacuum chamber with a base pressure of 0.015 mbar.

Initially, the wedge prism is kept in such a way as to have equal energy in two laser beams and is verified using an energy meter placed between the wedge prism and the focusing lens. The position of the wedge prism is adjusted to vary the input laser pulse energy on the targets.

The images of plume dynamics under different ratio of laser pulse energy are recorded using an intensified charge coupled device (ICCD) camera (ANDOR New iStar ICCD, Model no. DH334T-18U-E3) with a gate width of 20 ns and temporal resolution of 2 ns. Figure 2 represents the

Fig. 1 Angular target geometry: **a** schematic representation and **b** direct photograph of heterogeneous colliding laser-produced plasma

(a)   **(b)**

Fig. 2 Schematic representation of experimental setup

schematic representation of experimental setup for ICCD imaging. Two-lens setup is used to couple the plasma emission to the spectrometer (ANDOR SR-500i-B1-R) with wavelength resolution of 0.04 nm, to study the time-resolved optical emission. A dove prism is placed between the lenses to couple the desired region of plasma along the slit of the spectrometer. The slit width is fixed as 10 μm. A detailed diagram of experimental setup for spectrum recording is given in our previous work [21].

The deposition time is fixed as 2 h and the deposited films are analyzed using X-ray diffraction (XRD), field emission scanning electron microscopy (FESEM), energy-dispersive X-ray spectroscopy (EDAX), and atomic force microscopy (AFM).

3 Results and discussion

3.1 ICCD fast imaging

The temporally resolved 2D imaging of angular collision between two seed plasmas from different targets, including aluminum and copper, with varying input laser pulse energies is shown in Fig. 3. The dynamics of individual seed plasmas, its collision and expansion were clearly depicted in the ICCD images.

Figure 3a shows the time-resolved ICCD images of Al–Cu colliding laser-produced plasma with equal input laser energies of 65 mJ on each target. The individual seed plasmas expand freely at an initial time delay. Angular target geometry permits the interaction of fast-moving forward expansion velocity components of seed plasmas resulting in an earlier interaction of seed plasmas than of planar targets [8]. At 150 ns, the interaction region started to form at the collision front. From the image of 150 ns, it is clear that the Al seed plasmas reach the collision front faster than Cu plasma. It is due to the lower atomic mass of Al ions, which leads to its faster expansion, and also due to the higher ablation rate of Al. The thermal depth of a material is given by $\tau_T = \sqrt{D_T \tau_P}$, where D_T is the thermal diffusivity and τ_P is the laser pulse width. The thermal depth of Al is estimated as 0.91 μm, whereas for Cu, it is 1.05 μm. Lower thermal depth implies a greater ablation rate of Al compared to that of Cu [16].

At 200 ns, the two seed plasmas interact to form the stagnation region. Thus, the strong collision of Al and Cu
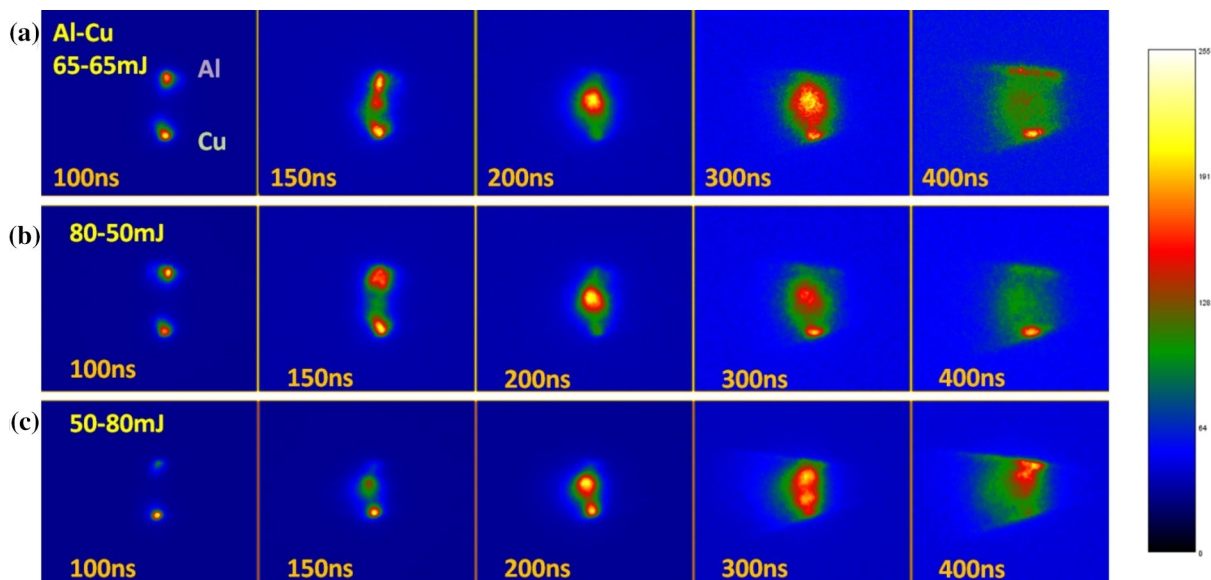
Fig. 3 Time-resolved ICCD images of Al–Cu colliding plasma with varying input laser energies: **a** 65–65 mJ, **b** 80–50 mJ and **c** 50–80 mJ on Al–Cu, respectively

plasmas occurs. As time elapses, the stagnation region expands, and the individual seed plasmas later interpenetrate each other.

Figure 3b and 3c represents the time-resolved ICCD images of Al–Cu collision with unequal input laser energies of 80–50 mJ and 50–80 mJ, respectively. In Fig. 3b, more laser energy is given for the ablation of Al plasmas, and therefore a significant contribution to the stagnation layer is due to Al plasmas. In Fig. 3c, since more laser energy is coupled to Cu target, more contribution in stagnation layer is from Cu plasma. At 150 ns, the Al seed plasma reaches the collision front and is found to be less intense. The heavier Cu plasma expands slower than Al plasma, making a slight shift in the interaction region closer to Cu target.

In all three cases, the individual seed plasmas expand, interact to form the stagnation region, and later interpenetrate each other. By varying the input laser energies, the time required for the interaction of seed plasmas, the shape and position of the stagnation region, and the interpenetration time get varied.

3.2 Optical emission spectroscopy

Time-resolved optical emission spectra of the colliding region of Al–Cu (65–65 mJ) at 10^{-2} mbar pressure range are shown in Fig. 4. Tracking the progression of the emission line in the stagnation region gives better insight into the evolution of various ionic stages in the stagnation region. The higher ionic states (Al III) exist only at the initial time delays and decrease more rapidly than the lower order ionic stages (Al II). At initial time delays, the kinetic energy of electrons is greater due to the absorption of laser energy, leading to an increase in collision frequency. Thus, the atoms or ions become more ionized due to the high collision rate, enhancing the intensity of ionic emission lines. In addition,

the higher ionization state and greater intensity of Al species compared to that of Cu is because of the localized heating that takes place on the Al target surface. Al with low ablation threshold needs only a small part of laser energy for the formation of the melted zone, and the remaining part of laser energy is utilized for the further heating the melted zone by inverse bremsstrahlung processes [16]. The details of major spectral lines covered in this experiment are given in Table 1.

Figure 5 depicts the optical emission spectra of both elements of Al and Cu in all three input laser energy variations. At equal laser energy ablation (65–65 mJ) of both elements, the intensity of ionic stages of Al is greater compared to that of Cu ionic lines. A higher ionic state like Al III also reveals the greater ionization of Al. In the case of Cu, due to the greater thermal depth, more laser energy is required for melting of the heavier target than that of heating processes [16]. It is the reason for observing atomic and lower state ionic lines of Cu with less intensity. Another reason for the enhancement of ionic lines of Al is due to the greater collision with the heavier Cu species. It is clear from Fig. 5 that there is a correlation between the laser energy and the intensity of spectral lines. By varying the laser energy on the desired target, it can tune the intensity of spectral lines at the collision front. Another interesting factor is the intensity increase of Al II line compared to Al III line in 80–50 mJ collision. In this case (80–50 mJ), the presence of Cu atoms or ions is less due to the less coupling of laser energy to the Cu target; therefore, the ionization rate with Cu atoms is less. In all other cases, Al III line dominates because of the greater ionization due to the collision with the heavier element. The collision between the lighter Al atoms with the heavier Cu atoms resulted in the gain of energy by the lighter atoms. It causes an enhancement of emission lines of Al and suppresses Cu emissions at lower wavelengths.
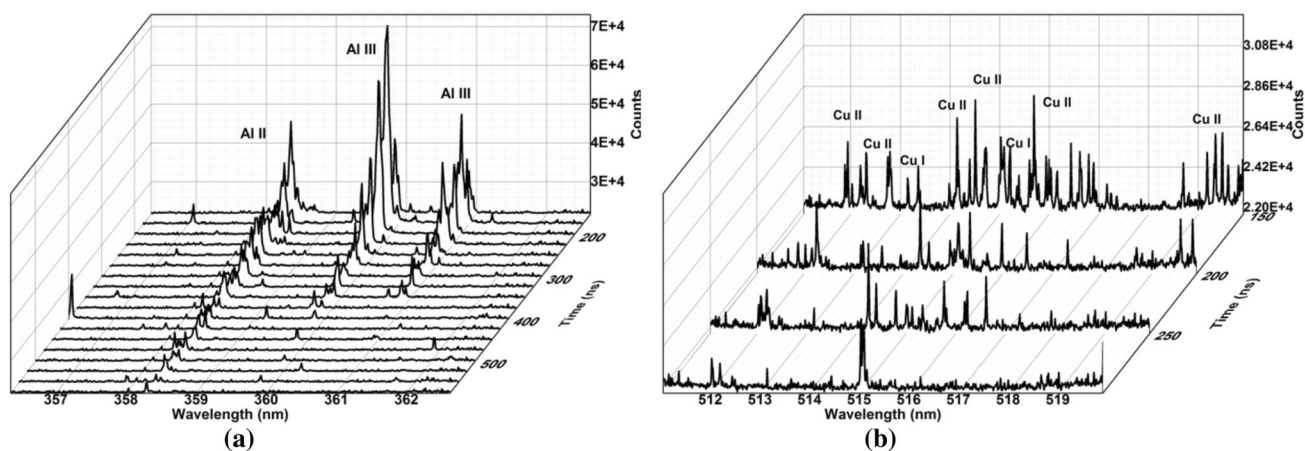
Fig. 4 Temporal variation of **a** Al II (358.65 nm), Al III (360.19 nm and 361.23 nm) and **b** Cu I (514.27 nm, 515.32 nm), Cu II (511.55 nm, 512.17 nm, 515.12 nm, 515.72 nm, 515.80 nm, 516.76 nm, 517.59 nm, 519.43 nm) of stagnation region

Table 1 Major emission lines of Al and Cu covered during this experiment

Spectral species	Wavelength (nm)	A_{ki} (s^{-1})	$E_i - E_j$ (cm^{-1})	Ionization energy (eV)
Al II	358.70	1.46e+09	95,550.51–123,420.45	18.82855
Al III	360.19	5.84e+07	115,958.50–143,713.50	28.44764
Al III	361.23	2.90e+08	115,958.50–143,633.38	28.44764
Al I	394.40	4.99e+07	0.000–25,347.756	5.985169
Cu II	491.89	2.6e+09	117,747.3504–138073.5826	20.29239
Cu II	492.14	2.6e+09	115,638.8036–135,952.279	20.29239
Cu II	493.72	1.1e+08	117,928.2197–138,176.8797	20.29239
Cu II	495.16	1.2e+08	115,638.8036–135,863.6857	20.29239
Cu II	496.98	1.7e+07	116,325.9148–136,441.817	20.29239
Cu II	497.12	1.7e+07	116,643.960–136,754.1104	20.29239
Cu II	498.10	3.0e+07	116,371.18040–136,441.817	20.29239
Cu II	501.26	9.6e+07	116,325.9148–136,269.9996	20.29239
Cu II	511.55	2.0e+06	118,071.302–118,071.302	20.29239
Cu II	512.17	2.0e+07	116,387.7873–135,910.7245	20.29239
Cu II	514.27	2.0e+07	45,820.94–65,259.93	20.29239
Cu I	515.32	6.0e+07	30,535.324–49,935.195	7.72638
Cu II	515.72	6.0e+07	116,375.406–135,760.1548	20.29239
Cu II	515.80	2.4e+07	116,576.5758–135,958.1919	20.29239
Cu II	516.76	2.4e+07	116,387.7873–135,733.433	20.29239
Cu II	517.59	2.4e+07	117,928.2197–137,242.914	20.29239
Cu II	519.43	2.4e+07	114,481.674–133,728.0387	20.29239

3.3 Band emission

Figure 6 depicts the molecular band emission of Cu_2 (A–X) in the stagnation region of Al–Cu (65–65 mJ) colliding plasma at 200 ns [16]. Copper having a greater ablation threshold, consumes a major part of the laser energy to form the melted zone, initially expanding isothermally and later adiabatically. Thus, the thermal energy of the plume is converted into kinetic energy and then the plasma cools down [22]. Molecular formation occurs due to the various recombination and condensation processes in the plasma. Since the Cu atoms possess a greater ablation threshold, most of the laser energy is consumed for the ablation and the rest for the ionization of the plume. Therefore, the Cu ions undergo recombination and lead to the formation of molecules [23].

The electron density is estimated using stark broadened line of Al I transition (394.40 nm). The other important broadening mechanisms includes Doppler and instrumental broadenings. The estimated spectral width due to Doppler effect is ~0.0004 nm, and is negligible. We use a minimum spectrometer slit width of 10 μm and at a resolution of 0.04 nm, therefore, the instrumental broadening is also negligible [21]. The relation between the full width at half maxima (FWHM) of Stark broadened line and the electron density is given in Eq. (1):

$$\Delta\lambda_{1/2} = 2W\left(\frac{n_e}{10^{16}}\right) \tag{1}$$

where $\Delta\lambda_{1/2}$ is the FWHM, W is the electron impact parameter and n_e is the electron density [24, 25].

The line intensity ratio method is used to estimate the electron temperature by assuming that the plasma is in local thermodynamic equilibrium (LTE) and by substituting the line intensities of Al II (358.65 nm and 466.30 nm) into the Boltzmann Eq. (2):

$$\frac{I_{ij}}{I_{kl}} = \frac{v_{ij}A_{ij}g_i}{v_{kl}A_{kl}g_k}\exp\left(\frac{-(E_i - E_k)}{K_BT_e}\right) \tag{2}$$

where I is the emission intensity due to the transition between two energy levels, A is the Einstein coefficient, v is the frequency of the spectral lines, g is the statistical weight of the energy level, K_B is the Boltzmann constant, E is the energy, T_e is the electron temperature, and the subscripts i, j, k, and l indicate the energy levels. The main criteria for LTE is

$$n_e \geq 1.6 \times 10^{12} T_e^{1/2}(\Delta E)^3 \tag{3}$$

where ΔE is the energy difference between the states. For the spectral line Al I (394.40 nm), it is about 2.185 eV and the lowest density value is about 1.7976×10^{15} cm^{-3}.
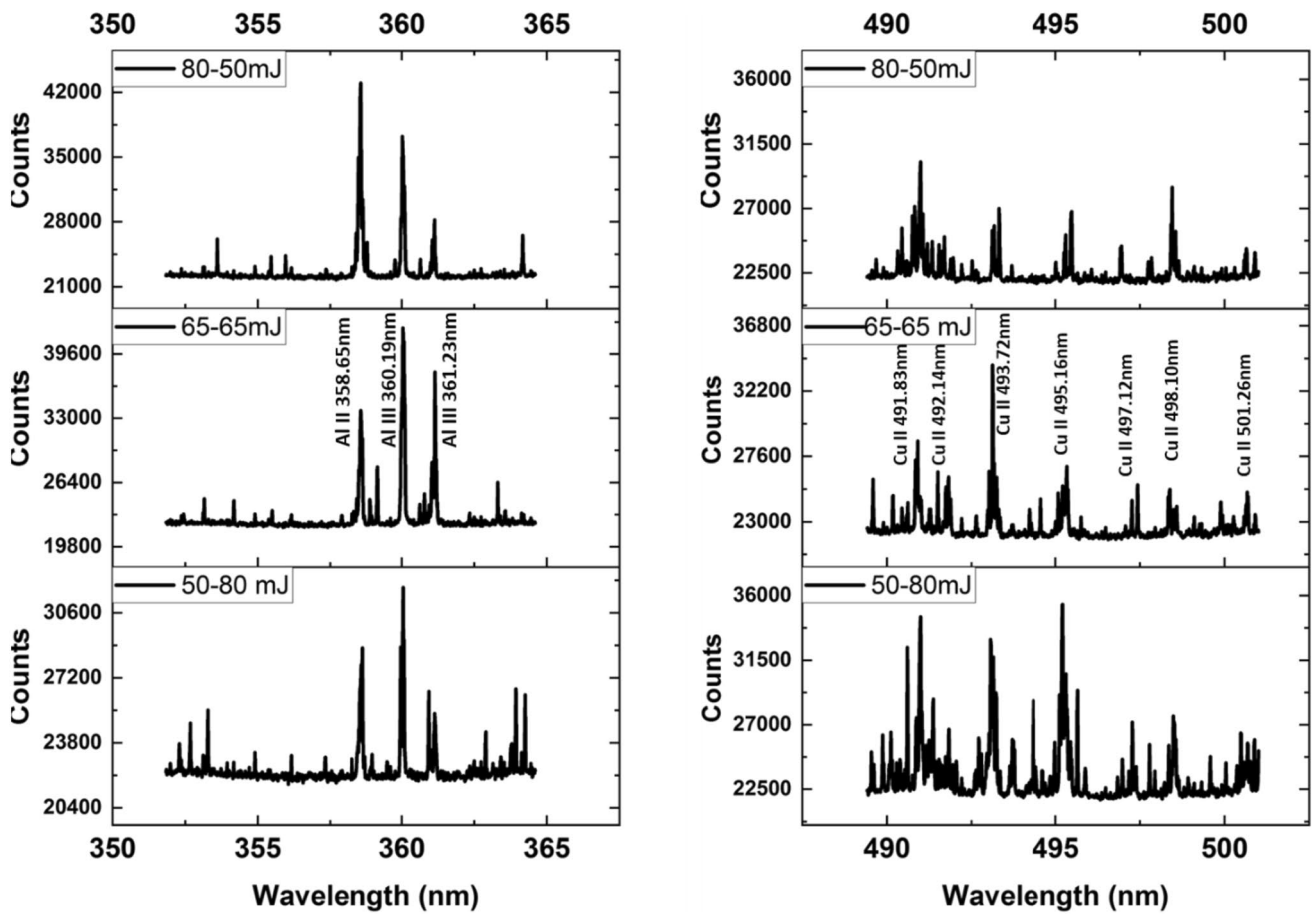
Fig. 5 Time-integrated emission spectra of Al II (358.65 nm), Al III (360.19 nm), Al III (361.23 nm), Cu I (493.69 nm), Cu II (491.83 nm, 492.14 nm, 493.72 nm, 495.16 nm, 496.98 nm, 497.12 nm, 498.10 nm, 501.26 nm) of stagnation region of Al–Cu colliding plasma at 10^{-2} mbar pressure range
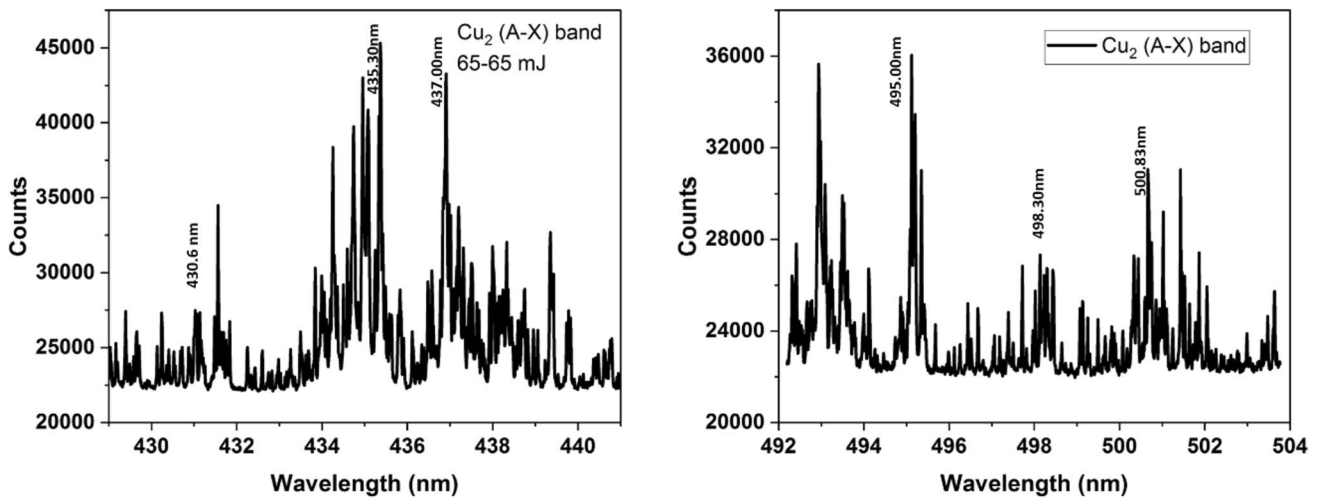

Fig. 6 Band emission spectra of Cu_2 (A–X) band in the stagnation region of Al–Cu (65–65 mJ) colliding plasma

Experimentally measured values of electron density are about $\sim 10^{16}$–10^{17} cm^{-3}, so the assumption of LTE is valid.

The temporal variation of electron density is given in Fig. 7a. The electron density is found to be greater for Al–Cu (80–50 mJ) case in which the aluminum is ablated more. Since the ablation threshold of aluminum is less, a major part of the laser energy is used for the ionization of the plume, and leads to the increase of electrons. The temporal variation of electron density is found to be equilibrating quickly, and it may be due to the early formation of the stagnation layer. The temporal variation of electron temperature is given in Fig. 7b. In all three cases, the electron temperature shows a decreasing nature. Pandey et al. [16] compared the temporal evolution of electron density and electron temperature of Cu–Ti colliding plasma at different pressures of oxygen ambient. They reported the increase of electron temperature and the higher value of electron density for a longer time with the increase of ambient pressure. Al-Juboori et al. [15] studied the effect of target geometry on the collision of Al–Si plasmas. Similar to our results, they also reported that the variation of electron density remains almost constant with an increase at initial time delays.

The angular target geometry is an effective method of mixing two metals with different physical and chemical properties. The significant advantage of this technique is the good control over the composition of the film. The deposition of intermetallic compounds is reported, whereas the engineering possibilities on the film composition are yet to be explored [13, 26]. To get the film, a glass substrate is kept at an off-axis of the expansion of the interaction region. The films deposited by varying the input laser energies are analyzed using techniques such as XRD, EDAX, FESEM, and AFM.

3.4 XRD analysis

Figure 8 shows the XRD pattern of Al–Cu films by varying the energy composition on Al–Cu (a) 65–65 mJ, (b) 80–50 mJ and (c) 50–80 mJ, respectively. The diffraction peaks 38.548°, 44.811°, 65.261°, and 78.382° corresponding to the planes (111), (200), (220), and (311), respectively, consist of combinations of Al–Cu including $Al_{0.99}Cu_{0.01}$ (PDF 01-074-5170), and 43.327° and 50.448° corresponding to the planes (111) and (200) consists of combinations of Al–Cu including $Al_{0.0565}Cu_{0.9434}$ (PDF 01-074-5169).

The reason for the two combinations may be due to the gradient mixing of two metals at the interaction region and the position of substrate is on the off-axis of expansion. $Al0.99Cu0.01$ intermetallic compound is formed by the mixing of Cu into the Al. The shift in the diffraction peak from pure Al diffraction data [19] clearly indicates the mixing of Cu into Al. The diffraction peak shifts are from 38.350° to 38.548°, 44.546° to 44.811°, 65.068° to 65.261°, and 78.075° to 78.382°. $Al_{0.0565}Cu_{0.9434}$ is formed by the mixing of Al into the Cu. The diffraction peak shifts from Cu are from 43.2° to 43.327° and 50.4° to 50.448°.

It is interesting to note that in all the three cases, the diffraction peaks obtained are of Al–Cu intermetallic compounds, and the intensity of combination varies with the variation of input laser energies.

By analyzing the diffraction pattern of film produced with the increase of laser energy on Al target (Al–Cu (80–50 mJ)), the intensity of diffraction peaks (38.548°,
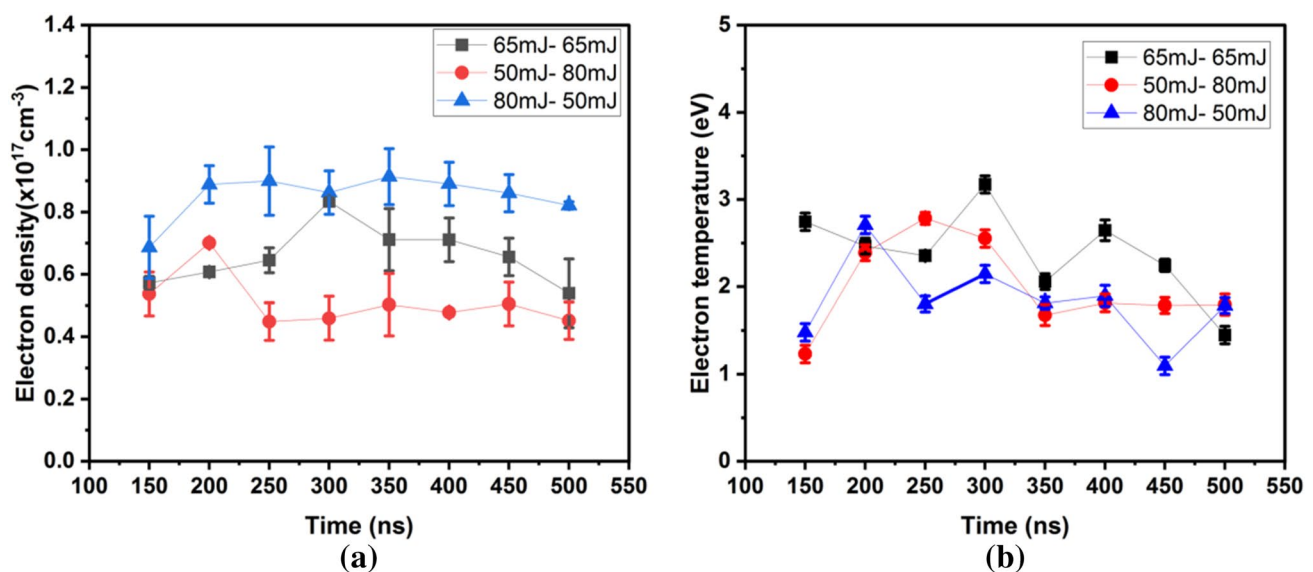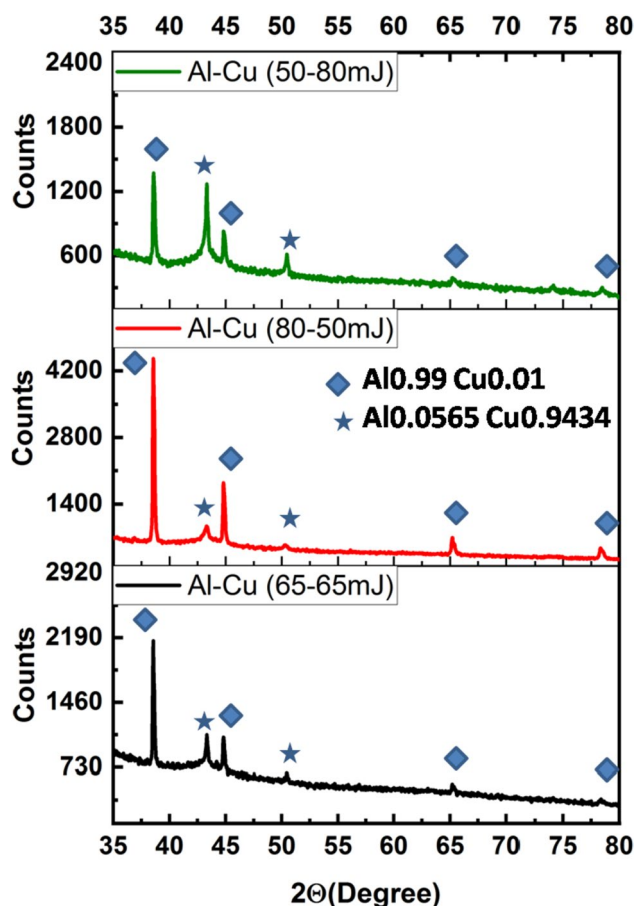

Fig. 7 Temporal distribution of **a** electron density and **b** electron temperature of stagnation region of different energy distributions

Fig. 8 XRD pattern of various energy composition of Al–Cu **a** 65–65 mJ, **b** 80–50 mJ and **c** 50–80 mJ

44.811°, 65.261°, and 78.382°) corresponding to $Al_{0.99}Cu_{0.01}$ increases, and the Al0.0565Cu0.9434 decreases. Likewise, by analyzing the diffraction peaks of Al–Cu (50–80 mJ), the intensity of diffraction peaks (43.327°, 50.448°) corresponding to $Al_{0.0565}Cu_{0.9434}$ increases, and the $Al_{0.99}Cu_{0.01}$ decreases.

The FESEM and EDAX pattern of Al–Cu (65–65 mJ) are shown in Fig. 9. Figure 9a shows the FESEM of film with equal ablation energy on targets. Some of the particles are spherical in nature and the size of the particles is not uniform. Figure 9b shows its EDAX pattern, which consists of Al and Cu having greater peak for Al. In equal energy of ablation also, Al with low ablation threshold get ablated more.

Figure 9c shows the FESEM of the film with ablation energy on targets of Al and Cu as 80 mJ and 50 mJ, respectively. More agglomeration of particles can be clearly visible in the FESEM, and the density of deposition is also greater. From Fig. 9d, EDAX patterns clearly indicate the increased presence of Al. More laser energy is coupled to the Al target, and due to the less ablation threshold, greater formation of

particles occurs. Figure 9e shows the FESEM of film with ablation energy on targets of Al and Cu as 50 mJ and 80 mJ, respectively. Figure 9f is the EDAX pattern of this combination, confirming the increased presence of Cu.

The surface topography of films of various mixing combinations is studied using AFM analysis. The two-dimensional (2D) and three-dimensional (3D) AFM images are used to measure the surface smoothness of the film. Figure 10a shows the 2D and 3D AFM image of Al–Cu with equal ablation energy on targets (65–65 mJ). These images consist of peak and valley structures with contrast colors. AFM images of film with increased amount of Al is shown in Fig. 10b and of Cu is shown in Fig. 10c. The AFM images show the broadening of lighter and darker regions, respectively. It is due to the agglomeration of more particles with increased concentration of Al and Cu [27]. The parameter RMS roughness provides information about the average surface roughness of the sample. The estimated surface roughness of the films are (a) Al–Cu (65–65 mJ) is 7.33 nm, (b) Al–Cu (80–50 mJ) is 25.3 nm and (c) Al–Cu (50–80 mJ) is 58.63 nm. Cu-dominated films have more roughness compared to other films.

Thus, the mixing of immiscible metals such as Al and Cu can be possible using the angularly colliding laser-produced plasma scheme and have a great control over the composition of deposited film.

4 Conclusions

The propagation dynamics of heterogeneous angularly colliding copper–aluminum laser-produced plasmas with varying input laser pulse energies are studied using fast imaging and optical emission spectroscopic techniques. The stagnation layer formed at the collision front consists of neutral and ionic species of both aluminum and copper species. The variations of spectral intensity of multispecies stagnation layer with respect to time and the variation in input laser pulse energies are studied. The variations in input laser pulse energies on each target can significantly influence the spectral composition in stagnation layer. Thus, the stoichiometry of composition in the stagnation layer can be controlled. The deposition of interaction region where the mixing of two different metals results in the formation of intermetallic compounds and the stoichiometry can be varied with input laser pulse energies. Thus, a one-step synthesis method of intermetallic compounds using a nanosecond laser ablation and special target geometry and without using any chemical reagents is proposed. Less time consuming and more provision to control the stoichiometry make it more special. Mixing of other immiscible metals used for various applications can also be synthesized by this method.
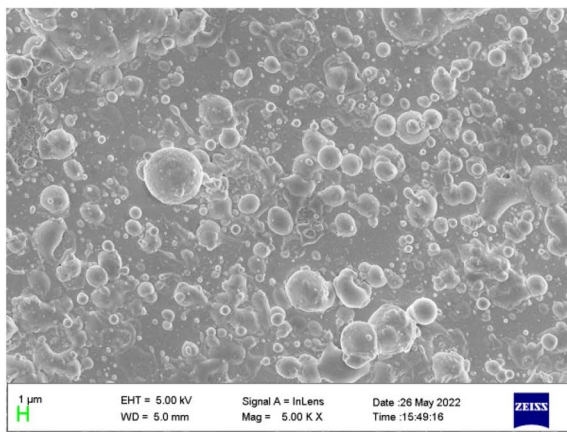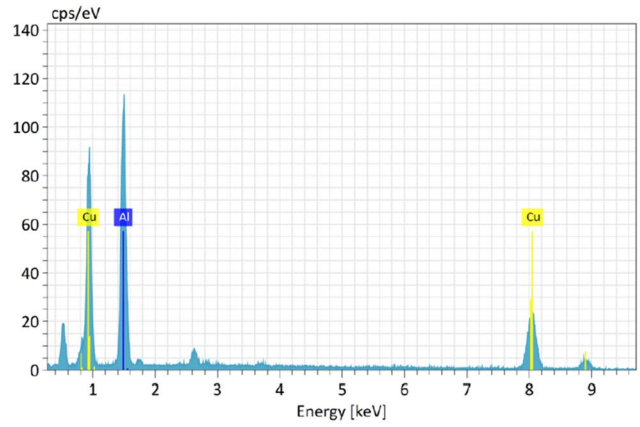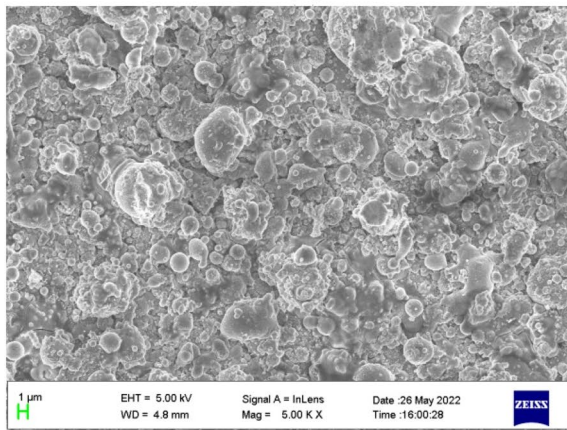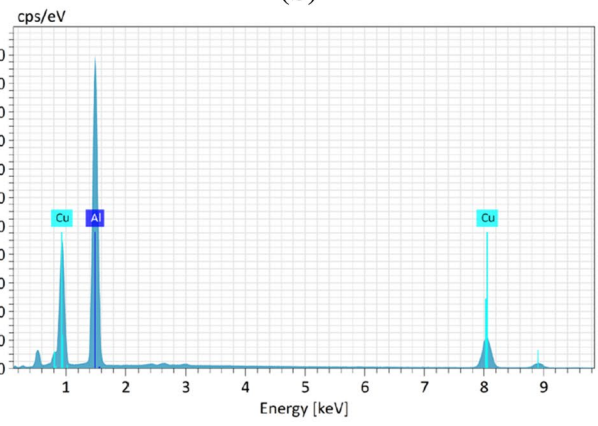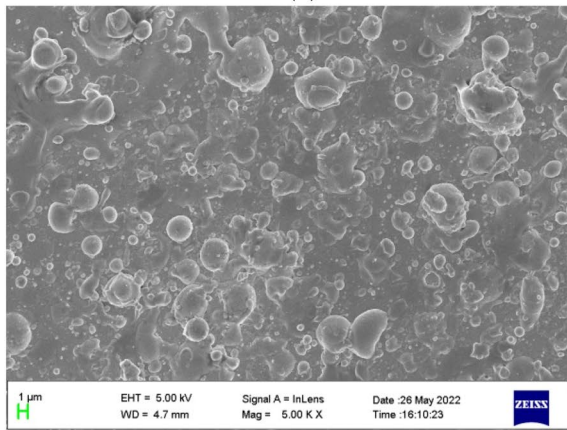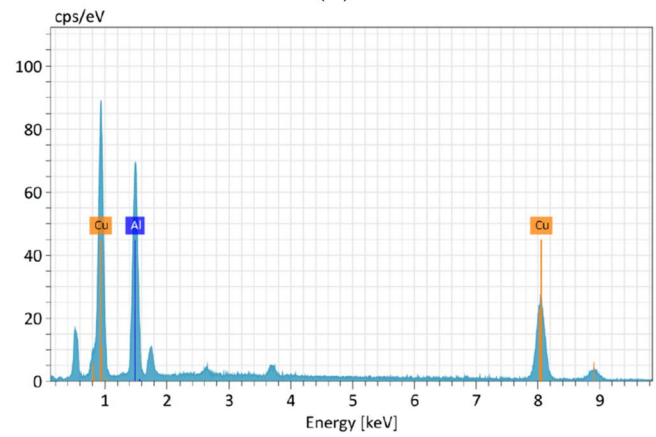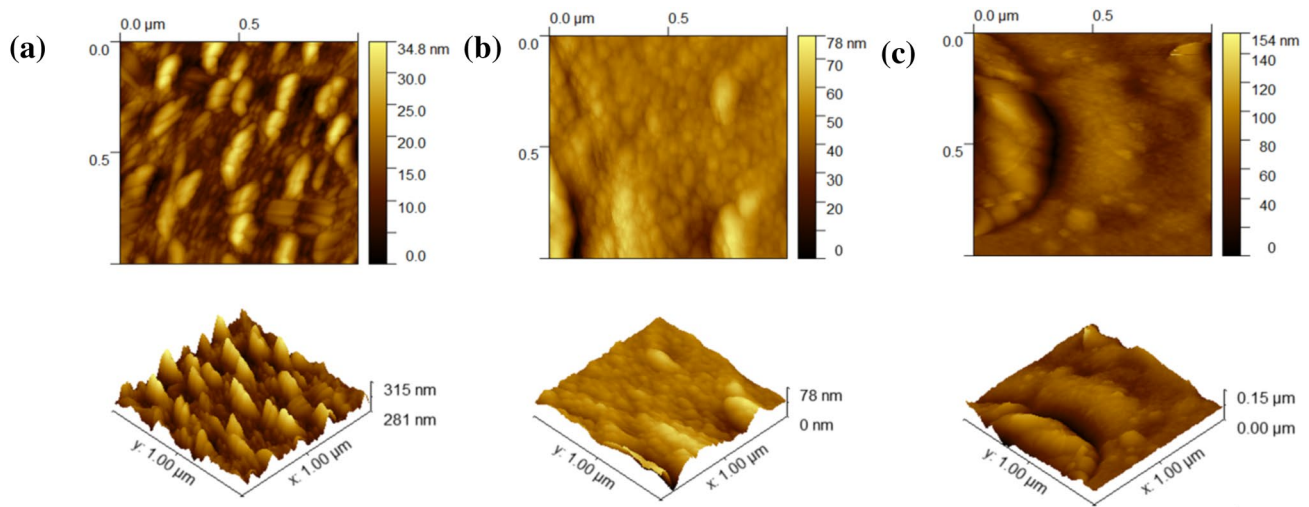
Fig. 9 FESEM and EDAX of various energy composition of Al–Cu **a** and **d** 65–65 mJ, **b** and **e** 80–50 mJ and **c** and **f** 50–80 mJ

Fig. 10 AFM images of films having various energy composition of Al–Cu **a** 65–65 mJ, **b** 80–50 mJ and **c** 50–80 mJ

Author contributions S. Shilpa: Writing – original draft, Methodology, Investigation, Formal analysis, Conceptualization. Pramod Gopinath: Conceptualization, Writing – review & editing, Validation, Supervision.

Data availability Data will be made available on request.

Declarations

Competing interests The authors declare no competing interests.

References

1. F. Colao, V. Lazic, R. Fantoni, S. Pershin, Spectrochim. Acta Part B **57**, 1167 (2002)
2. J. Schou, Appl. Surf. Sci. **255**, 5191 (2009)
3. S. Vijayalakshmi, M. George, J. Sturmann, H. Grebel, Appl. Surf. Sci. **127–129**, 378 (1998)
4. R.S. Craxton, K.S. Anderson, T.R. Boehly, V.N. Goncharov, D.R. Harding, J.P. Knauer, R.L. McCrory, P.W. McKenty, D.D. Meyerhofer, J.F. Myatt, A.J. Schmitt, J.D. Sethian, R.W. Short, S. Skupsky, W. Theobald, W.L. Kruer, K. Tanaka, R. Betti, T.J.B. Collins, J.A. Delettrez, S.X. Hu, J.A. Marozas, A.V. Maximov, D.T. Michel, P.B. Radha, S.P. Regan, T.C. Sangster, W. Seka, A.A. Solodov, J.M. Soures, C. Stoeckl, J.D. Zuegel, Phys. Plasmas **22**, 110501 (2015)
5. S. Matsuo, S. Juodkazis, H. Misawa, Appl. Phys. A **80**, 683 (2005)
6. A. Mondal, B. Kumar, R.K. Singh, H.C. Joshi, A. Kumar, Phys. Plasmas **26**, 022102 (2019)
7. H. Luna, K.D. Kavanagh, J.T. Costello, J. Appl. Phys. **101**, 033302 (2007)
8. S. Shilpa, P. Gopinath, Vacuum **198**, 110872 (2022)
9. S. Shilpa, P. Gopinath, Vacuum **208**, 111729 (2023)
10. M. Marklund, P.K. Shukla, Rev. Mod. Phys. **78**, 591 (2006)
11. R. Betti, O.A. Hurricane, Nat. Phys. **12**, 435 (2016)
12. V.I. Babushok, F.C. DeLucia, J.L. Gottfried, C.A. Munson, A.W. Miziolek, Spectrochim. Acta Part B **61**, 999 (2006)
13. A. Tselev, A. Gorbunov, W. Pompe, Rev. Sci. Instrum. **72**, 2665 (2001)
14. S. Shilpa, P. Gopinath, in *Proc. SPIE , Women Opt. Photonics India 2022*, edited by A. Mahadevan-Jansen, A. Pradhan, and S. N. Unni (SPIE, 2023), pp. 126380F–1.
15. H.M. Al-Juboori, N.A. Malik, T. McCormack, Phys. Plasmas **28**, 123515 (2021)
16. P.K. Pandey, R.K. Thareja, J.T. Costello, Phys. Plasmas **23** (2016).
17. P.K. Pandey, R.K. Thareja, R.P. Singh, J.T. Costello, Appl. Phys. B Lasers Opt. **124**, 1 (2018)
18. A. Gorbunov, A.A. Levin, A. Mensch, D.C. Meyer, A. Tselev, P. Paufler, W. Pompe, D. Eckert, Appl. Surf. Sci. **197–198**, 475 (2002)
19. L. Zhang, X. Gao, Z. Zhang, M. Zhang, Y. Cheng, J. Su, Sci. Rep. **6**, 31797 (2016)
20. S. Yan, Z. Li, L. Song, Y. Zhang, S. Wei, Opt. Lasers Eng. **161**, 107312 (2023)
21. S. Shilpa, P. Gopinath, Spectrochim. Acta Part B Atmos. Spectrosc. **207**, 106757 (2023)
22. P.K. Pandey, R.K. Thareja, J. Appl. Phys. **109**, 074901 (2011)
23. A.D. Sappey, T.K. Gamble, J. Appl. Phys. **72**, 5095 (1992)
24. H.R. Griem, Phys. Rev. **128**, 515 (1962)
25. S.S. Harilal, C.V. Bindhu, R.C. Issac, V.P.N. Nampoori, C.P.G. Vallabhan, J. Appl. Phys. **82**, 2140 (1997)
26. M.S.B. Darby, T.C. May-Smith, R.W. Eason, Appl. Phys. A Mater. Sci. Process. **93**, 477 (2008)
27. M. Sharma, P. Alves, L.M. Gando-Ferreira, J. Water Process Eng. **52**, 103487 (2023)